Dry synthesis of single-nanometer-scale Pt Si fine particles for electrocatalysis

doi: 10.1016/j.jelechem.2020.114492

Dry Synthesis of Single-Nanometer-Scale Pt-Si Fine Particles for Electrocatalysis

Naoto Todoroki, Shuntaro Takahashi, Kotaro Kawaguchi, Yusuke Fugane and Toshimasa Wadayama*

Graduate School of Environmental Studies, Tohoku University, Sendai 980-8579, Japan

Corresponding Author

*E-mail address: naoto.todoroki.b1@tohoku.ac.jp

Keywords

Platinum-silicone alloy; nanoparticles; arc-plasma deposition; electron-beam deposition; electrocatalysis; oxygen reduction reaction

Abstract

Single-nanometer-scale Pt-Si fine particles (Pt-Si NPs) were synthesized via the arc-plasma deposition of Si on a highly oriented pyrolytic graphite at a fixed substrate temperature of 600 ℃, followed by electron-beam deposition of Pt at the temperatures between 100 and 600 ℃ in ultra-high vacuum. X-ray diffraction patterns of the vacuum-synthesized Pt-Si NPs showed that a solid solution of Pt-Si was the major component of the particles. Minor diffraction peaks, due to the intermetallic compounds (Pt_3Si_1 and $Pt_{12}Si_5$), at the Pt-deposition temperature ($T_{sub\text{-}Pt}$) of 500 ℃, were also observed. Scanning tunneling microscopic images exhibited that Pt-Si NPs with an average diameter less than 10 nm were dispersed in the substrate at $T_{sub\text{-}Pt}$ temperatures up to 500 ℃. The Pt-Si NPs synthesized at a $T_{sub\text{-}Pt}$ of 300 and 450 ℃ showed 1.7 times higher initial mass activity for oxygen reduction reaction (ORR) compared to commercial carbon-supported Pt NPs catalysts and showed better electrochemical stability than pure Pt NPs. These results demonstrate that the arc-plasma deposition of Si NPs, followed by e-beam deposition of metal elements (Pt) in ultra-high vacuum is a new class dry-synthesis for the single-nanometer-scale fine particles of Pt-Si for electrocatalysis, e.g. ORR.

1. Introduction

Nanostructured Pt and its alloys of 3*d* transition metal elements have been used in various applications, such as electrocatalysis [1-4], electronics [5-7], and magnetics [8-10]. Pt alloys with semiconductor elements like Si (Pt silicides) have also been used as the contact electrode materials for electronic devices such as metal-oxide-semiconductor field-effect transistors (MOSFET) [6, 11-13] and phase-change random access memory (PCRAM) [14]. This is due to their low Schottky-barrier height [15] and their relatively high thermal and chemical stabilities [16]. A phase diagram of Pt-Si bimetallic system (Fig. S1) shows various line compounds such as Pt_3Si_1, $Pt_{12}Si_5$, Pt_2Si_1, Pt_6Si_5 and Pt_1Si_1, those of which reveal characteristic properties [17]. Particularly, the Pt_1Si_1 phase is known to be highly corrosion-resistant, even in aqua regia [18]. Therefore, Pt-Si can be used in electrochemical devices that operate in highly acidic environments. Indeed, the Pt-Si electrodes in acidic solutions were reported for methanol oxidation [19] and hydrogen evolution reactions [20].

Platinum-based nanoparticles (NPs) with single-nanometer-scale diameters (ca. less than 10 nm) are also of interest for electrocatalytic applications owing to their high specific surface area relative to their unit mass. Actually, Pt-based alloys as well as Pt-shell/transition-metal-core single-nanometer-scale fine particles have been intensively studied for highly-active oxygen reduction reaction (ORR) electrocatalysts [3, 21]. However, the average diameters of the reported Pt-Si NPs are greater than 10 nm [22-24]; a reduction in the particle diameter is needed to increase their surface area, improve their electrocatalytic activity, and make them suitable for applications like polymer electrolyte fuel cells (PEFCs) [25]. Generally, Pt and Pt-based alloy electrocatalysts are synthesized by the solution-reduction method, using metal-organic salts as precursors [26]. This approach enables precise control of the atomic composition [27], particle diameter [28], and

particle shape [29] through tuning of the reaction times, temperatures, and capping agents, etc. However, the solution-reduction method cannot be used to synthesize Pt-based alloy NPs with intrinsic semiconductor elements (Si, Ge), as complexes of these elements are very difficult to reduce in a solution phase.

In previous studies, we demonstrated that an arc plasma deposition (APD) method in ultra-high vacuum (UHV) is useful for synthesizing single nanometer-scale Pt-based alloys (Pt-Au, Pt-Ni, Pt-Co, Pt-Ta, Pt-Co-Au) [30-35]; Co-, Ta-nitrides [32]; and Ta-carbide NPs [36] for ORR cathodes used in PEFCs. Therefore, APD can be used to generate metal/alloy NPs by controlling pulse repetitions and arc voltages on various support materials. Because electro-conductive materials can be used as a target electrode (cathode) in APD, Si NPs can be deposited onto the material using an appropriate electro-conductive Si target. Therefore, in this study, we synthesized Pt-Si NPs on highly oriented pyrolytic graphite (HOPG) substrate in UHV via the APD of Si NPs. This was followed by electron-beam deposition of Pt. The initial ORR activities and durability of the synthesized samples were then investigated. The obtained average diameters of Pt-Si NPs were estimated to be less than 10 nm by controlling the substrate temperatures for Pt depositions lower than 500 ℃. Furthermore, These Pt-Si NPs showed higher ORR activity and durability compared to commercial Pt NPs supported on carbon black catalysts (Pt/C). The results demonstrate that this vacuum deposition procedure in UHV conditions makes it possible to synthesize Pt-Si NPs for ORR electrocatalysis in strong acid environments and other applications in vacuum and/or in air.

2. Experimental

All steps in the synthesis of the Pt-Si NPs were conducted in UHV (~10^{-8} Pa). A HOPG (TipsNano, 10 mm × 10 mm × t = 1 mm) substrate was used as the support substrate for the Pt-Si NPs. An illustration of the Pt-Si NPs synthesis is shown in Fig. 1. The HOPG substrate surface was first scraped using scotch tape in air, before being placed in a UHV chamber [33], where the surface was cleaned by annealing at 500 ℃ for 30 min. Next, Si was deposited on the surface of the HOPG substrate from boron doped Si target (ø10 mm × t = 18.5 mm, < 0.01 Ω· cm) using an APD gun (ADVANCE RIKO, APS-1) installed in the UHV chamber. The substrate temperature during the Si-APD and its amount were fixed at 600 ℃ and 0.097 μg cm^{-2}_{HOPG}, respectively. After deposition of the Si NPs, the substrate temperature was maintained at 600 ℃ for 30 min to agglomerate very fine atomic-level Si clusters. Pt (1.94 μg cm^{-2}_{HOPG}) was then deposited onto the HOPG containing the Si NPs using the electron-beam evaporation method at a substrate temperature (T_{sub-Pt}) of either 100, 300, 450, 500, or 600 ℃. From this stage, alloying temperatures of Si and Pt are described by *x* (T_{sub-Pt}) and synthesized samples were referred to as *x*-Pt-Si. The amounts of Pt and Si deposited on the substrate were estimated using a quartz micro-balance installed in the UHV chamber and the charged atomic ratio of the synthesized *x*-Pt-Si samples was fixed to be approximately Pt:Si = 3:1, based on the deposited amounts of Pt and Si. The crystal structures of the *x*-Pt-Si samples were analyzed using X-ray diffraction (XRD; SmartLab, Rigaku). The particle sizes of the *x*-Pt-Si NPs were evaluated using scanning tunneling microscopy (STM; Nanoscope V, Bruker) images obtained in air. Micro-structures and elemental distributions of the *x*-Pt-Si NPs were observed by scanning transmission electron microscopy (STEM; ARM-200F, JEOL) in conjunction with energy-dispersive spectroscopy (EDS). The chemical bonding states of the *x*-Pt-Si were analyzed using X-ray photoelectron spectroscopy (XPS; Thetaprobe,

ThermoFisherScientific).

To investigate the electrochemical characteristics, the *x*-Pt-Si samples were transferred into an electrochemical set-up using a purpose-built transfer vessel, to avoid exposing samples to the atmosphere. The cell was contained in a glovebox at 1 atm, and had been purged using N_2 [37]. A potentio-galvanostat (HZ-5000, Hokuto Denko), combined with a rotating disk electrode (RDE) system (HR-301, Hokuto Denko), and a purpose-built three-electrode glass cell were used to carry out electrochemical measurements. Pt-wire and reversible hydrogen electrodes (RHE), in a stream of H_2 gas, were used as counter and reference electrodes respectively. The *x*-Pt-Si samples were then immersed in 0.1 M $HClO_4$, prepared from perchloric acid (Ultra-pure, Kanto Chemical) and ultra-pure water (Milli-Q). The electrochemical surface conditioning procedures was conducted by applying potential cycles between 0.05 and 1.05 V vs. RHE for 100 cycles. Cyclic voltammetry (CV) was performed with a scan rate of 50 mV s^{-1}, without disk rotations, in a solution of 0.1 M $HClO_4$ that had been purged with N_2. The electrochemical surface area of Pt ($ECSA_{Pt}$) was estimated from the hydrogen desorption charges in the potential region from 0.08 to 0.38 V, assuming the charge for the monolayer hydrogen (210 μC cm^{-2}) [38]. After O_2 saturation of the 0.1 M $HClO_4$, linear sweep voltammetry (LSV) was conducted to evaluate the ORR activity of the *x*-Pt-Si samples, using the RDE with a disk rotation rate of 400−2500 rpm and with a potential sweep rate of 10 mV s^{-1}. The ORR mass activities (MA) and area-specific activities (SA) of the samples were estimated on the basis of kinetic current values (i_k) at 0.9 V vs. RHE from equations of (1) and (2), respectively, by considering of the Koutecky-Levich plots, deposited Pt mass (1.94 μg cm^{-2}_{HOPG}), and $ECSA_{Pt}$.

$$MA\ (A\ mg_{Pt}^{-1}) = i_k(mA)/deposited\ Pt\ mass\ (\mu g) \quad (1)$$

$$SA\ (mA\ cm_{ECSA}^{-1}) = i_k\ (mA)/ECSA_{Pt}\ (cm^2) \quad (2)$$

The ORR durability of the *x*-Pt-Si samples was evaluated based on changes in MA while applying square-wave potential cycles (PCs) between 0.6 and 1.0 V (3 s at each voltage), in a solution of, O_2-saturated 0.1 M $HClO_4$ at room temperature. Changes in sample surface morphologies and chemical bonding states, resultant from PCs, were investigated using STM and XPS.

3. Results and discussion

Fig. 2(a) shows the XRD patterns of the *x*-Pt-Si samples synthesized on the HOPG substrate. Two diffraction peaks around 39.8° and 85.6° are observed for all *x*-Pt-Si samples, and are assigned to the 111 and 222 reflections of Pt respectively [39]. These are also accompanied by relatively broad and weak peaks on either diffraction angle side. Additionally, diffraction peaks due to Si and its oxides (SiO or SiO_2) are not observed. These results suggest that the main structure of the *x*-Pt-Si samples is a Pt-rich Pt-Si solid-solution. Enlargement of the diffraction peaks around 39.8° (Fig. 2(b)) shows that the broad diffraction due to Pt 111 dominates the patterns of the 100- and 300-Pt-Si samples. By contrast, the 450-Pt-Si sample exhibits additional peaks at 38.0° and 41.5°. The intensities of these peaks increase for the 500- and 600-Pt-Si samples, accompanied by two new peaks at 35.8° and 42.5°. These additional peaks (35.8°, 38.0°, 41.5°, and 42.5°) are ascribed to orthorhombic Pt_3Si_1 [40]. Furthermore, it is observed that the 500- and 600-Pt-Si samples show an additional diffraction peak at 36.8°, corresponding to the 431 reflection of $Pt_{12}Si_5$ [19]. The XRD patterns presented in Fig. 2 indicate that the Pt-Si samples synthesized in conditions higher than 450 °C for $T_{sub\text{-}Pt}$ partly form intermetallic compounds of Pt_3Si_1 and $Pt_{12}Si_5$ in a solid solution matrix of Pt-Si; the Pt/Si molar compositions gradually decrease as $T_{sub\text{-}Pt}$ increases.

Fig. 3 shows STM images of the as-prepared *x*-Pt-Si samples. Insets are magnification images of each images. For the 100-Pt-Si sample, the average diameter of fine particles is

estimated to be ca. 3 nm. The diameters for the 300-, 450- and 500-Pt-Si samples are approximately the same, being ca. 7 nm. The sample prepared at $T_{sub\text{-}Pt}$ = 600 ℃ (600-Pt-Si) shows an increased agglomeration of the particles, when compared to other samples, resulting in an average particle diameter of ca. 14 nm. A high-angle-annular-dark-field (HAADF)-STEM image and STEM-EDS line profiles, of Pt (red) and Si (green), for the 300-Pt-Si sample are presented in Figs. 4(a) and 4(b) respectively. The lattice fringes of the individual particles in image (a) clearly reveal that the synthesized NPs are crystallized. The STEM-EDS line profiles for Pt (2.05 keV) and Si (1.74 keV) of the particle shown in (b) also indicate that the particle is not a Pt-Shell/Si(Pt-Si)-core-type nano-structures, but rather a solid solution of Pt-Si. Results of the STEM-EDS clearly show that the APD of Si NPs, followed by the electron-beam deposition of Pt, resulted in single-nanometer-scale, crystallized (not amorphous) Pt-Si fine particles. The average atomic ratio of the 300-Pt-Si samples estimated from the STEM-EDS mappings (Fig. S2) was approximately Pt:Si = 7:3, the ratio of which is close to the charged one (Pt:Si = 3:1).

X-ray photoelectron spectra of the Pt4*f* and Si2*s* bands of *x*-Pt-Si samples are summarized in Figs. 5(a) and 5(b) respectively. The Pt4*f* -7/2 band is located at ca. 72.0 eV, irrespective of the sample $T_{sub\text{-}Pt}$, and is 1.0 eV higher than that of the pure Pt (71.0 eV) [41]. Such the higher binding energy-shifts of the Pt4*f* bands are similar for various Pt-Si reported to date [11, 12, 42]. The Si2*s* bands of the corresponding samples appear around 154.4 eV, corresponding to those of SiO_2 [43]. As the dry synthesis and XPS measurements were performed in separate UHV chambers, the presence of SiO_2 could be the result of sample transfer between these chambers. It is expected that exposure of the sample to air, even at room temperature, would result in oxidation of the synthesized *x*-Pt-Si samples, particularly for Si. This result implies that further conclusions on the chemical bonding state of Si in the *x*-Pt-Si NPs cannot be made in this study. As shown in Fig.

5(c), the Pt/Si compositions in the near-surface region change as a function of the sample $T_{sub\text{-}Pt}$. The molar atomic ratios of the samples are estimated to be ca. Pt:Si=1:1 for the 100- and 300-Pt-Si samples. The Pt/Si ratios decrease with an increase of the $T_{sub\text{-}Pt}$: as for the 450-Pt-Si, the ratio can be estimated to be Pt:Si=1:3 and reaching a minimum ratio of Pt:Si=1:4, for the 600-Pt-Si. The results summarized in Fig. 5 indicate that thermal reactions of electron-beam deposited Pt with the pre-deposited Si should activate with increasing the $T_{sub\text{-}Pt}$, and that the Si tends to segregate to near-surface regions (within ca. 2 nm at the escape depth of Si2*s* photoelectrons) of the *x*-Pt-Si samples[44].

Fig. 6(a) shows cyclic voltammograms of the *x*-Pt-Si samples, (top panel; 100- and 300-Pt-Si, bottom 450-, 500-, and 600-Pt-Si) recorded in, N_2-purged 0.1 M $HClO_4$. All samples exhibit a typical CV response expected for hydrogen adsorption/desorption and interactions relating to oxygen species on the Pt electrode, in the potential regions between 0.05 and 0.35 V and 0.6 and 1.0 V respectively [45]. Because the CV features are sensitive to the top-surface elements, the CVs shown in Fig. 6(a) indicate that the top surfaces of the *x*-Pt-Si samples mainly comprise Pt atoms after the electrochemical surface cleaning procedure between 0.05 and 1.05 V for 100 cycles. As is summarized in (b), the $ECSA_{Pt}$ of the 300-Pt-Si sample decreases remarkably in comparison to the 100-Pt-Si sample. This can be explained either by the increase in the average diameters of the samples as judged by STM images (Fig. 3) or by the presence of surface Si-related species (Si and/or Si-oxides) as suggested by XPS spectra (Fig. 5). Because such the surface Si-related species should show no marked electrochemical features in the corresponding potential region (0.05–1.0 V) [46], the latter influence on the $ECSA_{Pt}$ is unclear yet. However, the XPS-estimated compositional changes of Pt and Si (Fig. 5(c)) clearly reveal the compositions for 100- and 300-Pt-Si samples are changed only slightly, suggesting that the former thermally induced

agglomeration should cause the difference in $ECSA_{Pt}$ for both the samples. Then, the $ECSA_{Pt}$ of the 450-Pt-Si sample is higher than the 300-Pt-Si one and the $ECSA_{Pt}$ gradually decrease with increasing the $T_{sub\text{-}Pt}$ up to 600 ℃. Except for the 600-Pt-Si sample whose average diameter is ca. twice as large as the 300- to 500-Pt-Si samples (STM images; Fig. 3), rather slight changes in $ECSA_{Pt}$ values for the 300-, 450-, and 500-Pt-Si samples suggest that the Pt/Si atomic ratios at the topmost surfaces in the solution of N_2-purged 0.1M $HClO_4$ are almost the same for the three samples, even though the different compositions of Pt and Si estimated in UHV by using XPS (Fig. 5(c)).

The LSV profiles, recorded in O_2-saturated 0.1 M $HClO_4$ at a potential sweep rate of 10 mV/s and the disk rotation of 1600 rpm, are summarized in Fig. 6(c). The ORR diffusion-limited potential regions (~6 mA/cm^2; 0.4–0.6 V) are present in all LSV scans of the *x*-Pt-Si samples. By contrast, the onset potentials for the kinetically controlled-current region (0.6–1.0 V) depend on the $T_{sub\text{-}Pt}$. As shown in Fig. 6(d), the initial MA of the *x*-Pt-Si samples synthesized under the $T_{sub\text{-}Pt}$ less than 500 ℃ are higher than the typical activity for the commercial Pt/C [47, 48]. Especially, both of the 300- and 450-Pt-Si samples show the MA and SA enhancement factors of 1.7 and 1.5, respectively, compared with the Pt/C. On the other hand, the SA of the 100-Pt-Si was much lower than the commercial Pt/C. The results suggest that the ORR activity enhancements of the *x*-Pt-Si samples, particularly 300- and 450-Pt-Si, mainly stem from by the thermal reaction of Pt with Si. As shown in Fig. 5(a), the peak positions of the Pt4*f* bands shift to higher binding energies by 1.0 eV, relative to pure Pt. This shift suggests the occurrence of charge transfer between Pt and Si. The charge transfers of Pt with other transition metal elements should cause the binding energy shift, not only of 4*f* orbitals, but also 5*d* orbitals [49] This directly correlates with the adsorption strength of oxygen-related species, O and/or OH. Indeed, the downward energy shift of the 5*d*

bands relative to the Fermi level causes a reduction in the adsorption strength of oxygen-related species on the surface of Pt [50]. This reduction in the adsorption strength should result in an increase in the ORR-active sites of the Pt in the kinetically controlled-current region. Therefore, the enhanced SA of the 300- and 450-Pt-Si samples might result from electronic modifications of the topmost-surface Pt atoms by the Si-related species located nearby, i.e., activity enhancements by the so-called ligand effect [51]. Alternatively, agglomerations of the Pt-Si NPs that induced by excess thermal energies (particularly for 600-Pt-Si) should result in reduction of both SA and MA.

Fig. 7 (a) shows the ORR activity changes for the *x*-Pt-Si samples by applying the PCs between 0.6 and 1.0 V (3s at each potential) in O_2-saturated 0.1 M $HClO_4$ (accelerated durability test protocol) [52]. The initial, pristine MA for all the *x*-Pt-Si samples were found to decrease with increasing the number of PCs. MA for the 300- and 450-Pt-Si samples, evaluated after the 10000 cycles, are 1.2 times higher than those of the commercial Pt/C than when they first started. This indicates an enhancement in the ORR durability. The STM images of the corresponding samples (300-, 450-Pt-Si), before and after the 10000 cycles, are summarized in Figs. 7 (b) and (c); corresponding STM images of pure Pt NPs, deposited on the HOPG by the APD, are also shown in (d) for a reference [30]. As shown, agglomerations are limited for both the 300- and 450-Pt-Si samples, with the average NP diameter increasing less than 0.5 nm as a result of the PCs. By contrast, the average diameters estimated after the 10000 cycles for the APD-prepared pure Pt NPs (d) are twice greater than those of the as-deposited Pt-Si samples. The results clearly show that superior electrochemical stability of the vacuum-synthesized Pt-Si NPs. Fig. 7 (e) show the XPS Pt4*f* and Si2*s* profiles of the 300-Pt-Si sample taken before and after the 10000 PC cycles. The Pt4*f* bands are shown to the lower-binding-energy-shift by 0.2 eV, as a result of the PCs

applications. This is accompanied by an opposite binding-energy-shift for the Si2s band, as well as a slight reduction in intensity. Although the chemical bonding states of Si cannot be discussed (mentioned above), the down shift of the Pt4*f* bands by the PCs should reflect a change in charge transfer between Pt and Si. It has been reported that very thin silica layers formed on the surface of Pt NPs, act as a physical barrier against the agglomeration of NPs. This directly correlates to the observed improvement in ORR durability [53]. The pH-potential diagram suggests that nanostructures of SiO_2, which might be generated as a result of the PC testing, are chemically stable at the potentials between 0.6 and 1.0 V vs. RHE in 0.1 M $HClO_4$ (pH = 1) [46]. Therefore, the Si oxides probably remain on the surfaces of the Pt-Si samples. Such the surface Si oxides might stabilize the surface Pt atoms of the *x*-Pt-Si samples and, thereby, improving ORR durability.

4. Conclusion

Single-nanometer-scale Pt-Si fine particles were successfully synthesized on a HOPG substrate via the UHV- process, the APD of Si NPs, followed by the electron-beam deposition of Pt at elevated substrate temperatures ($T_{sub\text{-}Pt}$). Results suggest that the crystal structures, and average diameters of the synthesized Pt-Si NPs depended upon the $T_{sub\text{-}Pt}$. Particularly, the single-nanometer-scale Pt-Si NPs that include intermetallic compounds of Pt_3Si_1 and $Pt_{12}Si_5$ in the Pt-Si solid solution matrix were generated at $T_{sub\text{-}Pt}$ values of 450 and 500 °C. X-ray photoelectron spectra of the UHV-synthesized *x*-Pt-Si samples revealed a shift of 1 eV to higher binding energies of Pt 4*f* bands, as compared to pure Pt. These results indicate that the electronic properties of the Pt were modified through a charge transfers between Pt and Si. Particularly, the 300- and 450-Pt-Si samples showed the MA and SA enhancement factors of 1.7 and 1.5, respectively, and better electrochemical stability (ORR durability) against the PCs in comparison to the APD-prepared Pt

NPs. The results demonstrate that the UHV-synthesized, single-nanometer-scale Pt-Si fine particles can be applicable not only for conducting electrode materials of the electronic devices used in vacuum or air but also for the electrocatalysts that require high-corrosion-resistance properties in strong acidic environments.

Acknowledgement

This study was supported by the New Energy and Industrial Technology Development Organization (NEDO) of Japan.

Appendix A. Supplementary data

Supplementary material related to this article can be found, in the online version. The materials contain additional information including a phase diagram of the Pt-Si bimetallic system, STEM-EDS mappings of the 300-Pt-Si sample and summary of detailed values of $ECSA_{-Pt}$, MA and SA.

Notes

The authors declare no competing financial interests.

References

[1] I.S. Kim, Z. Li, J. Zheng, A.E. Platero-Prats, A. Mavrandonakis, S. Pellizzeri, M. Ferrandon, A. Vjunov, L.C. Gallington, T.E. Webber, N.A. Vermeulen, R.L. Penn, R.B. Getman, C.J. Cramer, K.W. Chapman, D.M. Camaioni, J.L. Fulton, J.A. Lercher, O.K. Farha, J.T. Hupp, A.B.F. Martinson, Sinter-Resistant Platinum Catalyst Supported by Metal–Organic Framework, Angew. Chem. Int. Ed., 57 (2018) 909-913.
[2] J. Guo, C. Lin, C. Jiang, P. Zhang, Review on noble metal-based catalysts for formaldehyde oxidation at room temperature, Appl. Surf. Sci., 475 (2019) 237-255.
[3] R. Wang, H. Wang, F. Luo, S. Liao, Core–Shell-Structured Low-Platinum Electrocatalysts for Fuel Cell Applications, Electrochem. Energ. Rev., 1 (2018) 324-387.
[4] M. Liu, Z. Zhao, X. Duan, Y. Huang, Nanoscale Structure Design for High-Performance Pt-Based ORR Catalysts, Adv. Mater., 31 (2019) 1802234.
[5] R.T. Fryer, R.J. Lad, Synthesis and thermal stability of Pt3Si, Pt2Si, and PtSi films grown by e-beam co-evaporation, J. Alloy Compd., 682 (2016) 216-224.
[6] A.M. Thron, T.J. Pennycook, J. Chan, W. Luo, A. Jain, D. Riley, J. Blatchford, J. Shaw, E.M. Vogel, C.L. Hinkle, K. van Benthem, Formation of pre-silicide layers below Ni1−xPtxSi/Si interfaces, Acta Mater., 61 (2013) 2481-2488.
[7] P.L. Tam, L. Nyborg, Sputter deposition and XPS analysis of nickel silicide thin films, Surf. Coat. Technol., 203 (2009) 2886-2890.
[8] R. Huang, G.-F. Shao, Y. Zhang, Y.-H. Wen, Thermal Stability of Platinum–Cobalt Bimetallic Nanoparticles: Chemically Disordered Alloys, Ordered Intermetallics, and Core–Shell Structures, ACS Appl. Mater., 9 (2017) 12486-12493.
[9] O.D. Oniku, B. Qi, D.P. Arnold, Electroplated thick-film cobalt platinum permanent magnets, J. Magn. Magn. Mater., 416 (2016) 417-428.
[10] C. Di Paola, R. D'Agosta, F. Baletto, Geometrical Effects on the Magnetic Properties of Nanoparticles, Nano Lett., 16 (2016) 2885-2889.
[11] G. Larrieu, E. Dubois, X. Wallart, X. Baie, J. Katcki, Formation of platinum-based silicide contacts: Kinetics, stoichiometry, and current drive capabilities, J. Appl. Phys., 94 (2003) 7801-7810.
[12] Y.M. Woo, W.S. Hwang, W.J. Yoo, Formation of PtSi Schottky barrier MOSFETs using plasma etching, J. Vac. Sci. Technol. A, 33 (2015) 021307.
[13] J. Chan, M. Balakchiev, A.M. Thron, R.A. Chapman, D. Riley, S.C. Song, A. Jain, J. Blatchford, J.B. Shaw, K. van Benthem, E.M. Vogel, C.L. Hinkle, PtSi dominated Schottky barrier heights of Ni(Pt)Si contacts due to Pt segregation, Appl. Phys. Lett., 102 (2013) 123507.
[14] L.W.-W. Fang, R. Zhao, E.-G. Yeo, K.-G. Lim, H. Yang, L. Shi, T.-C. Chong, Y.-C. Yeo, Phase Change Random Access Memory Devices with Nickel Silicide and Platinum Silicide Electrode Contacts for Integration with CMOS Technology, J. Electrochem. Soc., 158 (2011) H232-H238.
[15] E. Alptekin, M.C. Ozturk, V. Misra, Tuning of the Platinum Silicide Schottky Barrier Height on n-Type Silicon by Sulfur Segregation, IEEE Electron Device Lett., 30 (2009) 331-333.
[16] W.J. Strydom, J.C. Lombaard, R. Pretorius, Thermal oxidation of the silicides CoSi2, CrSi2, NiSi2, PtSi, TiSi2 and ZrSi2, Thin Solid Films, 131 (1985) 215-231.
[17] F. Streller, R. Agarwal, F. Mangolini, R.W. Carpick, Novel Metal Silicide Thin Films by Design via Controlled Solid-State Diffusion, Chem. Mater., 27 (2015) 4247-4253.
[18] B. Liu, Y. Wang, S. Dilts, T.S. Mayer, S.E. Mohney, Silicidation of Silicon Nanowires by

Platinum, Nano Lett., 7 (2007) 818-824.
[19] A.A. Permyakova, B. Han, J.O. Jensen, N.J. Bjerrum, Y. Shao-Horn, Pt—Si Bifunctional Surfaces for CO and Methanol Electro-Oxidation, J. Phys. Chem. C, 119 (2015) 8023-8031.
[20] Y. Zhu, M. Yuan, L. Deng, R. Ming, A. Zhang, M. Yang, B. Chai, Z. Ren, High-efficiency electrochemical hydrogen evolution based on the intermetallic Pt2Si compound prepared by magnetron-sputtering, RSC Adv., 7 (2017) 1553-1560.
[21] C. Kim, F. Dionigi, V. Beermann, X. Wang, T. Möller, P. Strasser, Alloy Nanocatalysts for the Electrochemical Oxygen Reduction (ORR) and the Direct Electrochemical Carbon Dioxide Reduction Reaction (CO2RR), Adv. Mater., 0 (2018) 1805617.
[22] J.M. McEnaney, R.E. Schaak, Solution Synthesis of Metal Silicide Nanoparticles, Inorg. Chem., 54 (2015) 707-709.
[23] C.-T. Lin, Y.-W. Chen, J. Su, C.-T. Wu, C.-N. Hsiao, M.-H. Shiao, M.-N. Chang, Facile Preparation of a Platinum Silicide Nanoparticle-Modified Tip Apex for Scanning Kelvin Probe Microscopy, Nanoscale Res. Lett., 10 (2015) 401.
[24] J. Zhu, G.A. Somorjai, Formation of Platinum Silicide on a Platinum Nanoparticle Array Model Catalyst Deposited on Silica during Chemical Reaction, Nano Lett., 1 (2001) 8-13.
[25] C. Zhang, X. Shen, Y. Pan, Z. Peng, A review of Pt-based electrocatalysts for oxygen reduction reaction, Front. Energy, 11 (2017) 268-285.
[26] M.B. Gawande, A. Goswami, T. Asefa, H. Guo, A.V. Biradar, D.-L. Peng, R. Zboril, R.S. Varma, Core-shell nanoparticles: synthesis and applications in catalysis and electrocatalysis, Chem. Soc. Rev., 44 (2015) 7540-7590.
[27] B. Han, C.E. Carlton, A. Kongkanand, R.S. Kukreja, B.R. Theobald, L. Gan, R. O'Malley, P. Strasser, F.T. Wagner, Y. Shao-Horn, Record activity and stability of dealloyed bimetallic catalysts for proton exchange membrane fuel cells, Energ. Environ. Sci., 8 (2015) 258-266.
[28] J. Quinson, M. Inaba, S. Neumann, A.A. Swane, J. Bucher, S.B. Simonsen, L. Theil Kuhn, J.J.K. Kirkensgaard, K.M.Ø. Jensen, M. Oezaslan, S. Kunz, M. Arenz, Investigating Particle Size Effects in Catalysis by Applying a Size-Controlled and Surfactant-Free Synthesis of Colloidal Nanoparticles in Alkaline Ethylene Glycol: Case Study of the Oxygen Reduction Reaction on Pt, ACS Catal., 8 (2018) 6627-6635.
[29] L. Gan, S. Rudi, C. Cui, M. Heggen, P. Strasser, Size-Controlled Synthesis of Sub-10 nm PtNi3 Alloy Nanoparticles and their Unusual Volcano-Shaped Size Effect on ORR Electrocatalysis, Small, 12 (2016) 3189-3196.
[30] S. Takahashi, H. Chiba, T. Kato, S. Endo, T. Hayashi, N. Todoroki, T. Wadayama, Oxygen reduction reaction activity and structural stability of Pt-Au nanoparticles prepared by arc-plasma deposition, Phys. Chem. Chem. Phys., 17 (2015) 18638-18644.
[31] N. Todoroki, T. Kato, T. Hayashi, S. Takahashi, T. Wadayama, Pt–Ni Nanoparticle-Stacking Thin Film: Highly Active Electrocatalysts for Oxygen Reduction Reaction, ACS Catal., 5 (2015) 2209-2212.
[32] S. Takahashi, N. Takahashi, N. Todoroki, T. Wadayama, Dealloying of Nitrogen-Introduced Pt–Co Alloy Nanoparticles: Preferential Core–Shell Formation with Enhanced Activity for Oxygen Reduction Reaction, ACS Omega, 1 (2016) 1247-1252.
[33] S. Takahashi, N. Takahashi, N. Todoroki, T. Tanabe, T. Wadayama, Oxygen Reduction Reaction Activity and Durability for Pt/TaNx Model Catalysts Fabricated in Ultra-High-Vacuum, ECS Trans., 75 (2016) 821-826.
[34] S. Takahashi, N. Todoroki, R. Myochi, T. Nagao, N. Taguchi, T. Ioroi, F.E. Feiten, Y. Wakisaka, K. Asakura, O. Sekizawa, T. Sakata, K. Higashi, T. Uruga, Y. Iwasawa, T. Wadayama,

Effective surface termination with Au on PtCo@Pt core-shell nanoparticle: Microstructural investigations and oxygen reduction reaction properties, J. Electroanal. Chem., 842 (2019) 1-7.
[35] F.E. Feiten, S. Takahashi, O. Sekizawa, Y. Wakisaka, T. Sakata, N. Todoroki, T. Uruga, T. Wadayama, Y. Iwasawa, K. Asakura, Model building analysis – a novel method for statistical evaluation of Pt L3-edge EXAFS data to unravel the structure of Pt-alloy nanoparticles for the oxygen reduction reaction on highly oriented pyrolytic graphite, Phys. Chem. Chem. Phys., (2020) DOI:10.1039/C1039CP06891K.
[36] R. Myochi, T. Nagao, Y. Fugane, S. Takahashi, N. Todoroki, T. Wadayama, Oxygen Reduction Reaction Properties for Dry-Process Synthesized Pt/TaCx Nanoparticles, ECS Trans., 86 (2018) 519-524.
[37] T. Wadayama, N. Todoroki, Y. Yamada, T. Sugawara, K. Miyamoto, Y. Iijama, Oxygen reduction reaction activities of Ni/Pt(111) model catalysts fabricated by molecular beam epitaxy, Electrochem. Commun., 12 (2010) 1112-1115.
[38] S. Trasatti, O.A. Petrii, Real surface area measurements in electrochemistry, Pure Appl. Chem., 63 (1991) 711-734.
[39] E. Antolini, F. Cardellini, Formation of carbon supported PtRu alloys: an XRD analysis, J. Alloy Compd., 315 (2001) 118-122.
[40] R.T. Fryer, R.J. Lad, Electronic and thermal properties of stoichiometric Pt3Si films grown by co-evaporation, J. Mater. Sci., 53 (2018) 3524-3536.
[41] K.-R. Lee, I.P. Lin, H.-T. Chang, S.-W. Lee, Platinum silicide formation on Si1−yCy epitaxial layers, J. Alloy Compd., 574 (2013) 415-420.
[42] S.J. Morgan, R.H. Williams, J.M. Mooney, An XPS study of thin Pt and Ir silicide overlayer formation on Si(100)2 X 1 surfaces, Appl. Surf. Sci., 56-58 (1992) 493-500.
[43] L.F. Edge, D.G. Schlom, R.T. Brewer, Y.J. Chabal, J.R. Williams, S.A. Chambers, C. Hinkle, G. Lucovsky, Y. Yang, S. Stemmer, M. Copel, B. Holländer, J. Schubert, Suppression of subcutaneous oxidation during the deposition of amorphous lanthanum aluminate on silicon, Appl. Phys. Lett., 84 (2004) 4629-4631.
[44] U. Diebold, L. Zhang, J.F. Anderson, P. Mrozek, Surface segregation of silicon in platinum(111), J. Vac. Sci. Technol. A, 14 (1996) 1679-1683.
[45] F.J. Vidal-Iglesias, R.M. Arán-Ais, J. Solla-Gullón, E. Herrero, J.M. Feliu, Electrochemical Characterization of Shape-Controlled Pt Nanoparticles in Different Supporting Electrolytes, ACS Catal., 2 (2012) 901-910.
[46] M. Pourbaix, J.A. Franklin, Atlas of Electrochemical Equilibria in Aqueous Solutions, Pergamon Press, Oxford, England, 1966.
[47] H. Kwon, M.K. Kabiraz, J. Park, A. Oh, H. Baik, S.-I. Choi, K. Lee, Dendrite-Embedded Platinum–Nickel Multiframes as Highly Active and Durable Electrocatalyst toward the Oxygen Reduction Reaction, Nano Lett., 18 (2018) 2930-2936.
[48] C.M. Pedersen, M. Escudero-Escribano, A. Velázquez-Palenzuela, L.H. Christensen, I. Chorkendorff, I.E.L. Stephens, Benchmarking Pt-based electrocatalysts for low temperature fuel cell reactions with the rotating disk electrode: oxygen reduction and hydrogen oxidation in the presence of CO, Electrochim. Acta, 179 (2015) 647-657.
[49] T. Toda, H. Igarashi, H. Uchida, M. Watanabe, Enhancement of the Electroreduction of Oxygen on Pt Alloys with Fe, Ni, and Co, J. Electrochem. Soc., 146 (1999) 3750-3756.
[50] J.K. Nørskov, J. Rossmeisl, A. Logadottir, L. Lindqvist, J.R. Kitchin, T. Bligaard, H. Jónsson, Origin of the Overpotential for Oxygen Reduction at a Fuel-Cell Cathode, J. Phys. Chem. B, 108 (2004) 17886-17892.

[51] T. Bligaard, J.K. Nørskov, Ligand effects in heterogeneous catalysis and electrochemistry, Electrochim. Acta, 52 (2007) 5512-5516.
[52] A. Ohma, K. Shinohara, A. Iiyama, T. Yoshida, A. Daimaru, Membrane and Catalyst Performance Targets for Automotive Fuel Cells by FCCJ Membrane, Catalyst, MEA WG, ECS Trans., 41 (2011) 775-784.
[53] S. Takenaka, H. Miyamoto, Y. Utsunomiya, H. Matsune, M. Kishida, Catalytic Activity of Highly Durable Pt/CNT Catalysts Covered with Hydrophobic Silica Layers for the Oxygen Reduction Reaction in PEFCs, J. Phys. Chem. C, 118 (2014) 774-783.

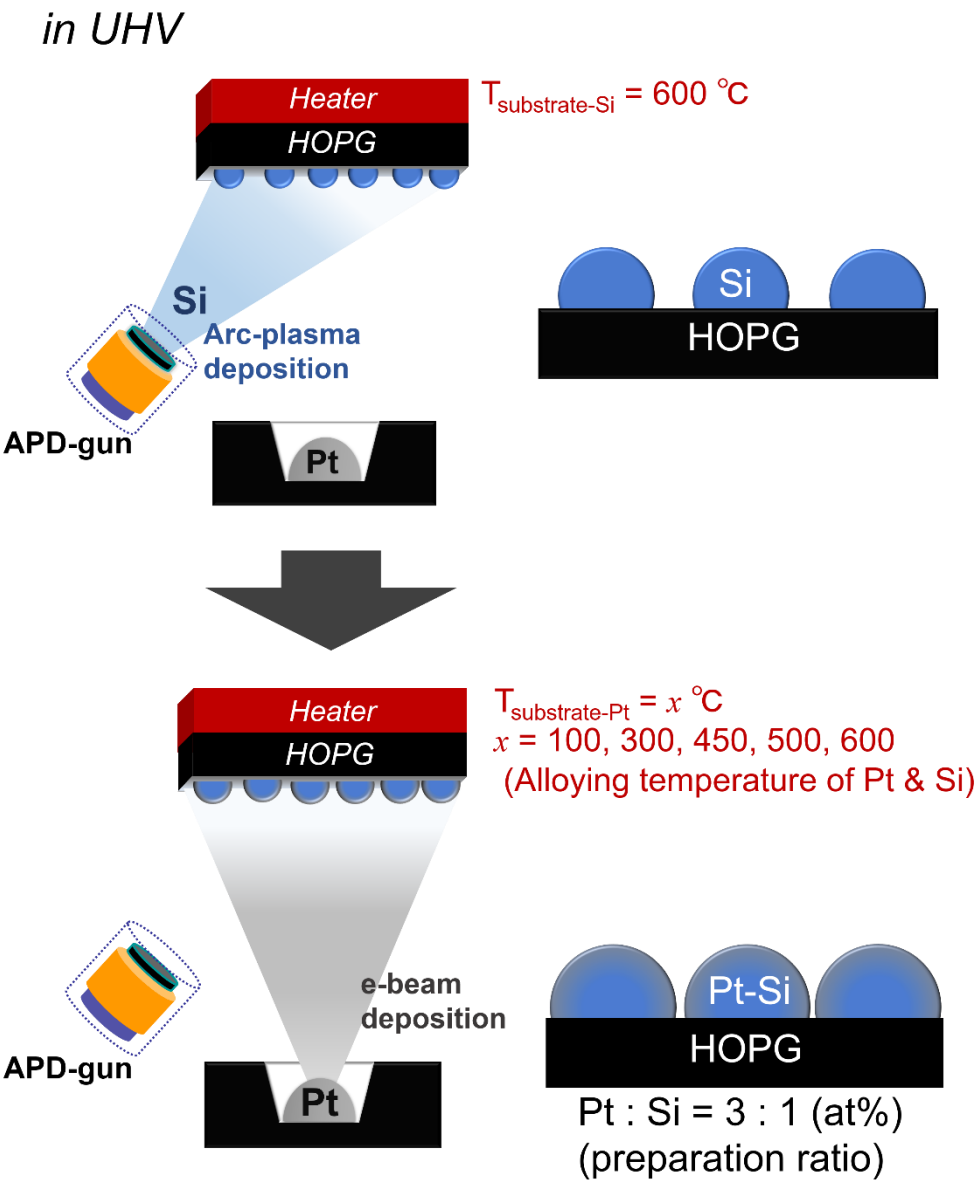

Fig. 1. Fabrication procedures of the *x*-Pt-Si samples.

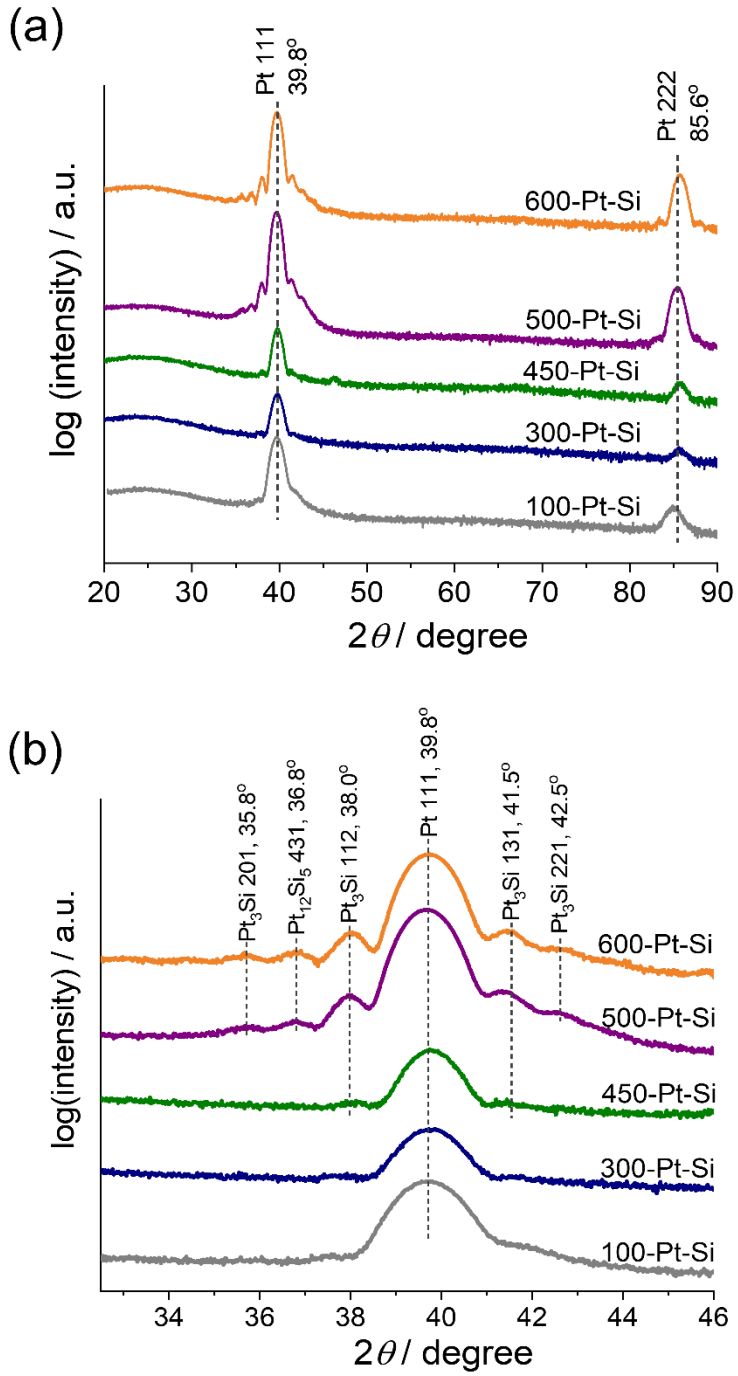

Fig. 2. (a) XRD patterns of the *x*-Pt-Si samples, collected from 20° to 90° in 2θ. (b) Enlarged view around the Pt 111 diffraction (2θ=39.8°).

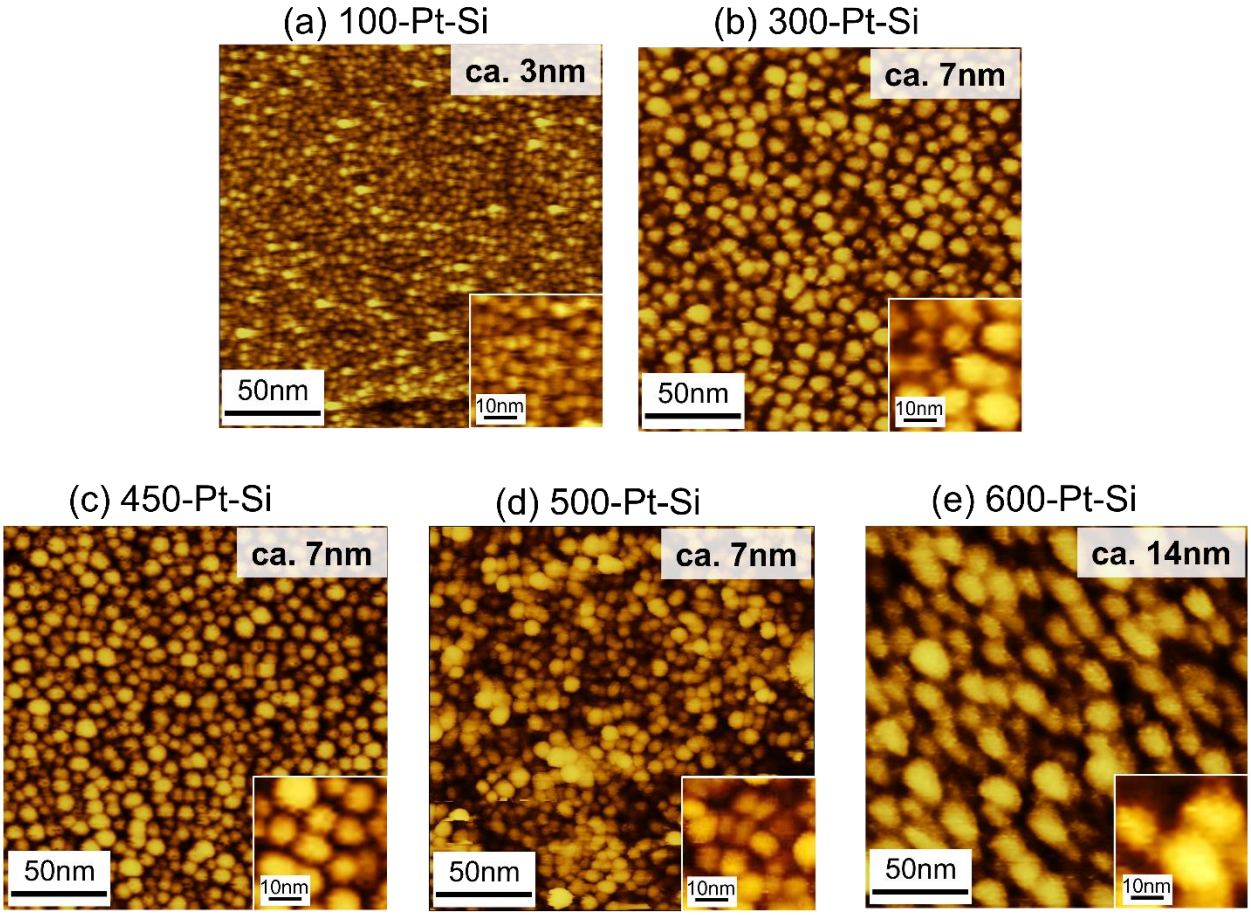

Fig. 3. STM images of as-prepared *x*-Pt-Si samples (*x*=100-, 300-, 450-, 500-, and 600 °C). Average diameters of the fine particles are displayed in the top right of each image. Insets are magnifications of the each STM images.

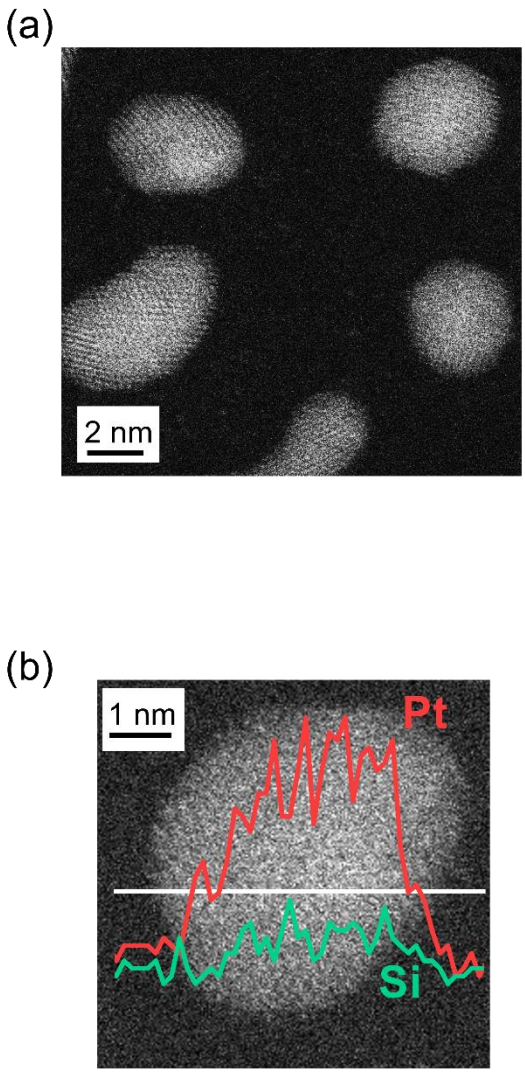

Fig. 4. HAADF-STEM image (a) and STEM-EDS line profile (b) of the 300-Pt-Si sample; Pt and Si are shown in red and green respectively, along the white horizontal line.

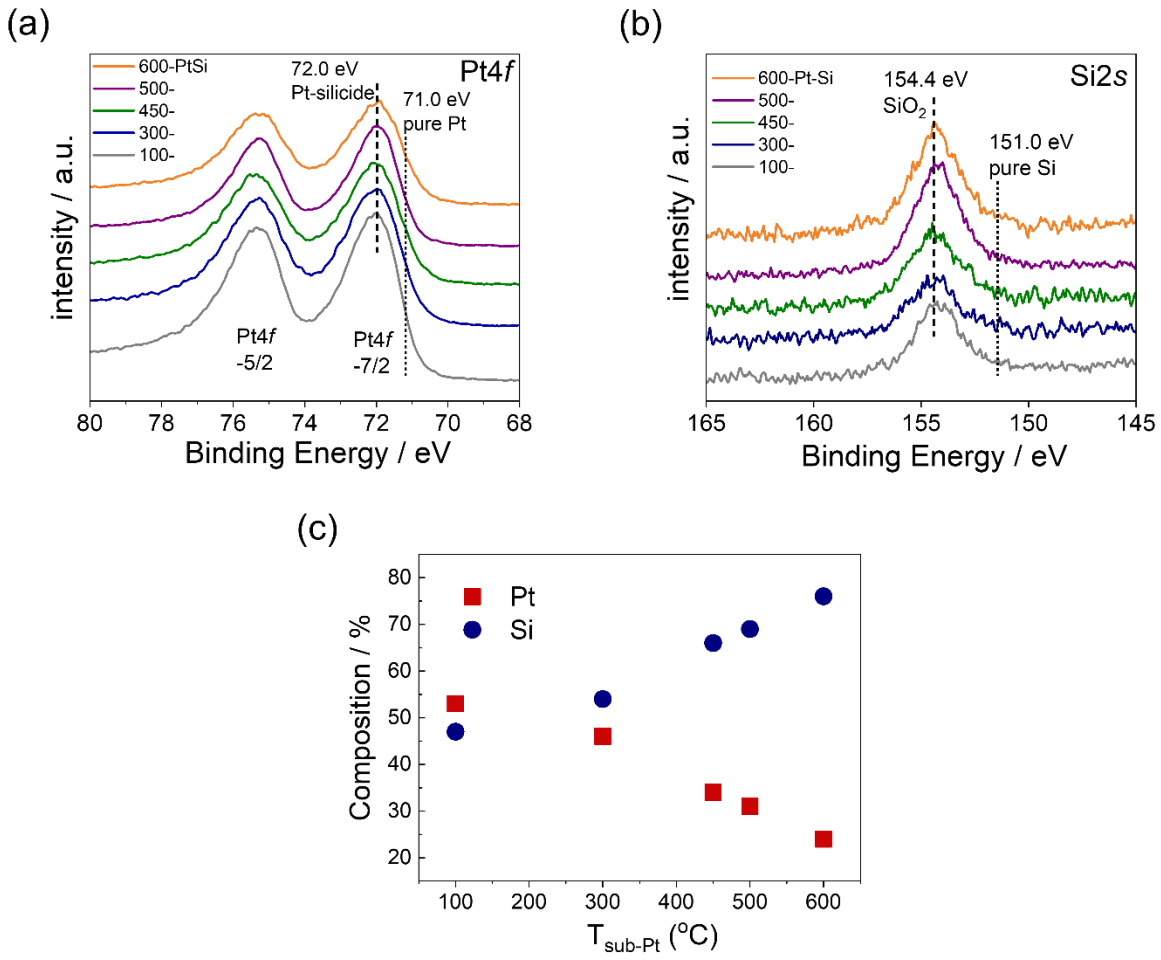

Fig. 5. XPS profiles of the Pt4*f* (a) and Si2*s* (b) bands of the *x*-Pt-Si samples. (b) XPS-estimated compositional changes of Pt (red square) and Si (navy circle), as a function of sample $T_{sub\text{-}Pt}$.

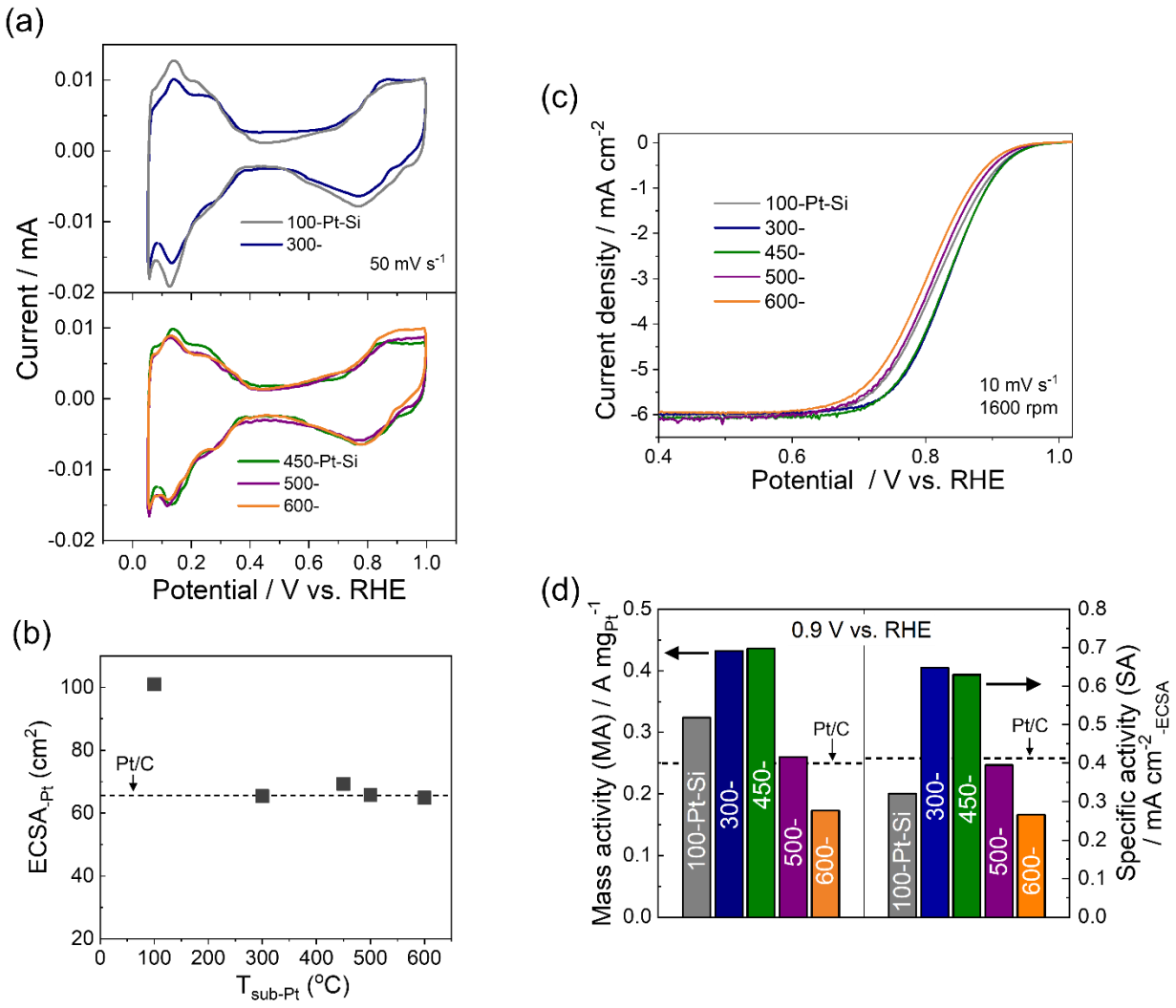

Fig. 6. Initial electrochemical properties of *x*-Pt-Si samples: (a) Cyclic voltammograms recorded in N_2-purged 0.1 M $HClO_4$. (b) Electrochemical surface area of Pt estimated from cyclic voltammograms. (c) Linear sweep voltammograms for the ORR recorded in O_2-saturated 0.1 M $HClO_4$ with a disk rotation of 1600 rpm. (d) Mass activities and specific activities (j_k) for ORR at 0.9 V vs. RHE.

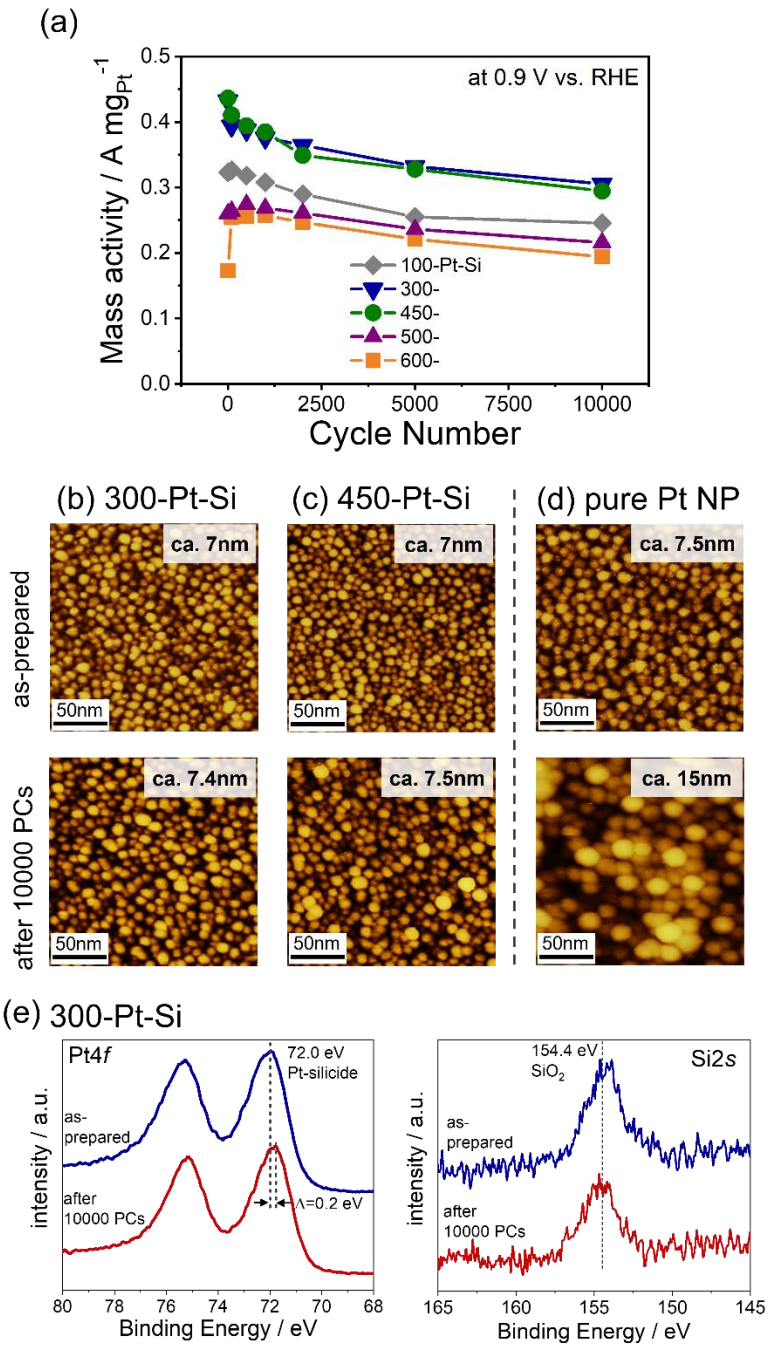

Fig. 7. (a) ORR mass activity changes during PCs between 0.6 and 1.0 V in O_2-saturated 0.1 M $HClO_4$. STM images before and after 10000 PC cycles of 300- (b) and 450-Pt-Si (c) samples, and APD-prepared pure Pt NPs. (e) XPS profiles of Pt 4*f* and Si 2*s* bands before and after 10000 PC cycles of the 300-Pt-Si sample.